Article

Change Detection in SAR Images Based on Deep Semi-NMF and SVD Networks

Feng Gao †, Xiaopeng Liu †, Junyu Dong *, Guoqiang Zhong and Muwei Jian

College of Information Science and Engineering, Ocean University of China, Qingdao 266100, China; gaofeng@ouc.edu.cn (F.G.); simonlinux@sohu.com (X.L.); gqzhong@ouc.edu.cn (G.Z.); jianmuwei@ouc.edu.cn (M.J.)

* Correspondence: dongjunyu@ouc.edu.cn; Tel.: +86-532-6678-1123

† These authors contributed equally to this work.

Abstract: With the development of Earth observation programs, more and more multi-temporal synthetic aperture radar (SAR) data are available from remote sensing platforms. Therefore, it is demanding to develop unsupervised methods for SAR image change detection. Recently, deep learning-based methods have displayed promising performance for remote sensing image analysis. However, these methods can only provide excellent performance when the number of training samples is sufficiently large. In this paper, a novel simple method for SAR image change detection is proposed. The proposed method uses two singular value decomposition (SVD) analyses to learn the non-linear relations between multi-temporal images. By this means, the proposed method can generate more representative feature expressions with fewer samples. Therefore, it provides a simple yet effective way to be designed and trained easily. Firstly, deep semi-nonnegative matrix factorization (Deep Semi-NMF) is utilized to select pixels that have a high probability of being changed or unchanged as samples. Next, image patches centered at these sample pixels are generated from the input multi-temporal SAR images. Then, we build SVD networks, which are comprised of two SVD convolutional layers and one histogram feature generation layer. Finally, pixels in both multi-temporal SAR images are classified by the SVD networks, and then the final change map can be obtained. The experimental results of three SAR datasets have demonstrated the effectiveness and robustness of the proposed method.

1. Introduction

Remote sensing image change detection is the process of identifying land cover changes by using remotely-sensed images of the same geographical area at different times [1]. It is of high practical value in a large number of applications in diverse disciplines, such as crop growth monitoring [2], urban sprawl detection [3,4], hazard assessment [5], and snow cover monitoring [6]. Therefore, change detection has become an attractive research topic in remote sensing communities recent years.

With the development of Earth observation programs, more and more multi-temporal synthetic aperture radar (SAR) images are available [7]. Owning to the fact that SAR images can be obtained independently of atmospheric and sunlight conditions, SAR images are more suitable than optical or hyperspectral images to be employed in change detection. Hence, in recent decades, SAR images have been successfully applied in environmental monitoring, urban studies, and forest monitoring. However, change detection based on SAR images encounters more difficulties than that based on optical or hyperspectral images due to the presence of speckle noise [8,9].

In spite of the difficulties brought about by speckle noise, tremendous progress has been made in recent years, and many SAR image change detection techniques have shown impressive performance. These techniques can be categorized into two main research streams: supervised approaches and unsupervised approaches [10]. Supervised approaches need to utilize reliable training samples to train a classifier, which will be used to classify each pixel into a changed class or an unchanged class. The samples are selected based on prior knowledge or manual labeling. On the other hand, unsupervised approaches make direct comparisons between multi-temporal images to identify the changes. Due to the fact that reliable samples are not always available, unsupervised approaches are more preferable to supervised ones. Unsupervised approaches are widely used in remote sensing communities in practice. Therefore, this paper focuses on unsupervised SAR image change detection.

Existing unsupervised SAR image change detection techniques are mainly based on difference image (DI) analysis. Generally, these techniques are often comprised of two steps [8]: (1) DI generation by using various kinds of operators, and (2) classification of the DI into changed and unchanged classes. Since these techniques are based on DI analysis, the quality of DI is very important and affects the final change detection results. The common technique used to generate a DI is the log-ratio operator [11,12], since the log-ratio operator is widely acknowledged to be robust to calibration and radiometric errors.

In the DI classification step, the thresholding method and clustering method are generally used. The thresholding method is the most intuitive way to analyze the DI. Bruzzone et al. [13] assumed that the conditional density functions of the changed and unchanged classes can be modeled by Gaussian distributions. The Expectation-Maximization (EM) iterative algorithm is used to find the optimal threshold. Later, a similar framework was proposed in [14] by using the Kittler-Illingworth (K&I) threshold selection criterion. Celik [15] proposed an automatic threshold technique based on Bayes theory in the wavelet domain instead of the spatial domain. These thresholding methods have achieved good performance when changed and unchanged classes have distinct modes in the histogram of DI, respectively. However, they often encounter difficulties when changed and unchanged classes are strongly overlapped or their statistical distribution cannot be modeled accurately [16]. Therefore, clustering methods are proposed to take local region information into account. In [17], a reformulated fuzzy local information c-means cluster algorithm (RFLICM) is proposed to classify the DI based on local information. The algorithm does not need to estimate the distribution of changed and unchanged classes, and it is robust to speckle noise due to the use of local information. Celik [18] proposed an efficient method for change detection by using PCA and k-means clustering. In this method, the DI is divided into overlapping image blocks. A feature vector space is created by projecting the block around each pixel into eigenvector space, and then the k-means clustering algorithm is employed to cluster the feature vector space into changed and unchanged classes. Li et al. [19] proposed a novel change detection method based on two-level clustering. Two-level clustering is designed in Gabor feature space by successively combining the first-level fuzzy c-means (FCM) clustering with the second-level nearest neighbor rule. In the optical image change detection community, the contextual information is an important factor in DI analysis. Lv and Zhong [20] proposed a multi-feature probabilistic ensemble conditional random field model for DI analysis. In this method, morphological operators are used to keep the main structure of the changed regions, and spatial contextual information is considered by the pairwise potential designed in the conditional random field model.

Several recent publications have formulated unsupervised change detection problem as an incremental learning problem. To be specific, the process of change detection simulates the learning process of humans [21]. Humans learn to understand the world by prior knowledge provided by predecessors, through which each forms his own interpretations of the world. Similarly, the change detection task can be formulated as the following steps: First, an initial change map is generated by thresholding or clustering algorithms. Second, samples are selected from the change map and fed into a learning system as prior knowledge. Finally, the system gives its own interpretations of multi-temporal SAR images and generates a final change map. Liu et al. [21] established a deep neural network using stacked Restricted Boltzmann Machines (RBM) to analyze the DI. In [22], a joint classifier based on FCM

was designed to select reliable samples, and then a two-layer RBM network was established for image change detection. Liu et al. [23] proposed a deep network comprised of one convolutional layer and several coupling layers. The network performs well in heterogeneous optical and SAR image change detection. In the optical image change detection community, deep architectures have been successfully exploited for feature representations in change detections. Zhang et al. [24] proposed a framework for multi-spatial resolution image change detection, which incorporates deep architecture-based feature learning. In the framework, stacked denoising autoencoders are integrated for learning high-level features from raw image data. Zhong et al. [25] proposed a method based on pulse-coupled neural networks (PCNN) and normalized moment of inertia (NMI) feature analysis. The method can provide better performance for high spatial resolution optical images. In deep learning, the hierarchical structure can learn different features at different layers, and these features can represent the change information between multi-temporal images. Therefore, the available methods that depend on deep learning can obtain excellent results. In a recent technical tutorial [26], Zhang et al. systematically reviewed state-of-the-art deep learning techniques in remote sensing data analysis. They pointed out that deep learning can automatically obtain high-level semantic features from raw data in a hierarchical manner, while traditional shallow models can hardly uncover high-level data representations.

Deep learning methods may perform poorly when the number of training samples is relative small. Generally, millions of training samples are necessary to obtain a model with powerful feature representation capability. However, this is nearly impossible for the task of SAR image change detection [27,28]. Though deep learning-based methods are promising, the problem of limited samples must be solved. Zou and Shi [29] proposed SVD networks, which are designed based on the recent popular convolutional neural networks to solve the problem of ship detection in optical images. These networks can efficiently learn features from remote sensing images. Inspired by Zou's method [29], in this paper, we put forward a simple change detection scheme for SAR images based on deep semi-nonnegative matrix factorization (Deep Semi-NMF) and SVD networks. Inspired by the aforementioned methods, this paper formulates the change detection problem as an incremental learning problem. Deep Semi-NMF is first utilized for feature extraction, and the hierarchical FCM clustering algorithm is used to select sample pixels that have high probabilities of being changed or unchanged. Then, image patches centered at these sample pixels are generated, and these patches are used to train a model by SVD networks. Finally, pixels in the multi-temporal images are classified by the model. The SVD network classification result and the pre-classification result are combined to form the final change detection result.

The main contribution of this paper can be summarized as the following two aspects. First, we put forward a pre-classification scheme based on Deep Semi-NMF and hierarchical FCM to obtain labeled samples of high accuracy. Second, we propose a classification model based on SVD networks for change detection. SVD networks can learn nonlinear relations from multi-temporal SAR images, and are able to suppress the noisy unchanged regions. The proposed change detection method makes no rigorous assumption and is unsupervised. Therefore, it can be easily adapted for data across different SAR sensors.

This paper is organized into four sections. Section 2 elaborates on the framework of the proposed change detection method. Section 3 analyzes the accuracy of change detection on several real SAR datasets. Section 4 first analyzes the influence of related parameters on the performance of change detection, and then discusses the performance of the proposed method with closely related methods. Finally, Section 5 makes concluding remarks on the proposed method.

2. Change Detection Methodology

Let us consider two co-registered intensity SAR images I_1 and I_2 acquired over the same geographical area at two different times. Both images are of $M \times N$ pixels. The purpose of change detection is to produce a difference image that can represent the change information between the two

times in the scene. The final output of the change detection analysis is to produce a binary image associated with changed and unchanged pixels by dividing the difference image into two classes.

Figure 1 shows the pipeline of the proposed change detection method. The proposed method is mainly comprised of three steps:

Step 1—Pre-classification based on Deep Semi-NMF and hierarchical FCM. The log-ratio operator is first utilized to generate the log-ratio image. Then, Deep Semi-NMF is adopted for feature extraction. The hierarchical FCM algorithm is utilized for feature classification and pixels in the log-ratio image are partitioned into three groups: the changed class Ω_c, the unchanged class Ω_u, and the intermediate class Ω_i. Pixels from Ω_c and Ω_u are selected as training samples for SVD networks.

Step 2—Training a classifier by SVD networks. Image patches centered at interested pixels obtained in Step 1 are generated from multi-temporal SAR images. Pixel-wise features are extracted directly from these patches. Then, SVD networks comprised of two SVD convolutional layers and one histogram feature generation layer are built. By using SVD networks, a classifier based on pixel-wise patch features is trained.

Step 3—Classification of changed and unchanged pixels by using the pretrained classifier. Pixels belonging to the intermediate class Ω_i are classified into changed and unchanged class by using the classifier obtained in Step 2. Then, the classification result and the pre-classification result generated in Step 1 are combined to form the final change map.
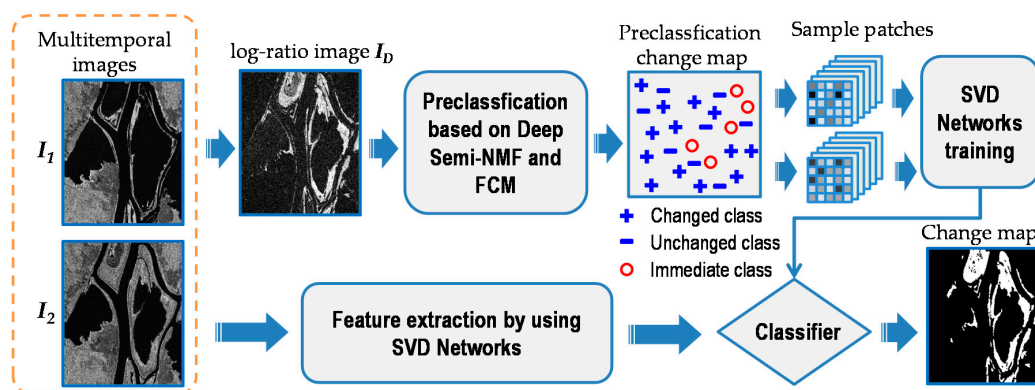

Figure 1. Flow chart of the proposed change detection method.

Section 2 is organized as follows. Section 2.1 gives the detailed description of pre-classification based on Deep Semi-NMF and hierarchical FCM clustering. Section 2.2 introduces the process of classification by using SVD networks.

2.1. Pre-classification Based on Deep Semi-NMF and Hierarchical FCM Clustering

The first step of the proposed change detection method is pre-classification, which aims to select reliable samples for SVD networks. This subsection details the pre-classification process based on Deep Semi-NMF and hierarchical FCM. Section 2.1.1 reviews the Deep Semi-NMF briefly. Section 2.1.2 introduces the detailed strategy for pre-classification.

2.1.1. Deep Semi-NMF

Nonnegative Matrix Factorization (NMF) is useful to find representations of nonnegative data. It can approximate a nonnegative matrix with the product of two low-dimensional nonnegative matrices. NMF allows only additive combinations, and therefore the nonnegative constraints of NMF lead to a parts-based representation [30]. The parts-based property makes NMF suitable for a broad range of applications, such as hyperspectral image unmixing [31,32], face recognition [33], and image classification [34]. In [27], Zhang et al. presented an elegant solution for high dimensional

remote sensing data analysis. They pointed out that matrix factorization is an important tool to extract significant features for remote sensing data analysis. Therefore, it is plausible to use matrix factorization for SAR image feature explorations.

Given an $m \times n$ nonnegative data matrix V and a pre-specified positive integer r, NMF aims to find two nonnegative matrices $W \in \mathbb{R}^{m \times r}$ and $H \in \mathbb{R}^{r \times n}$, such that:

$$V \approx WH. \tag{1}$$

It should be noted that r is a pre-specified positive integer. The value of r is relatively small, so that $(m + n)r < mn$. Thus, H is considered as a new representation of the original data matrix V. W is considered as the mapping between the new representation H and the original data matrix V.

In many real world applications, the data matrix V often has mixed signs. Considering this, Ding et al. [35] proposed the Semi-NMF, which can impose non-negativity constraints only on the second factor H, but allows mixed signs in both the data matrices V and W. The Semi-NMF has been considered to be equivalent to k-means clustering, and it has been expected to perform better than k-means clustering particularly when the input data is not distributed in a spherical manner.

It is considered that the mapping W contains complex hierarchical and structural hidden representations. By further factorizing the mapping W, we can automatically learn the hidden representations and obtain better higher-level feature representations of the original data matrix V. Inspired by this, Trigeorgis et al. [36] proposed Deep Semi-NMF, which applies Semi-NMF to a multi-layer structure in order to learn hidden representations of the original data matrix. Specifically, the input data matrix is factorized into $m + 1$ factors as follows:

$$V^{\pm} = W_1^{\pm} W_2^{\pm} \cdots W_m^{\pm} H_m^{+}, \tag{2}$$

Here, $W_m^{\pm}$ means that a matrix is allowed to have mixes signs, and H_m^{+} means that a matrix is comprised of strictly nonnegative components. This can be viewed as learning a hierarchical structure of features, with each layer learning a representation suitable for clustering according to the different attributes of the input data. The input data can be represented by a hierarchy of m layers as follows:

$$\begin{aligned} H_{m-1}^{+} &\approx W_m^{\pm} H_m^{+}, \\ &\vdots \\ H_2^{+} &\approx W_3^{\pm} \cdots W_m^{\pm} H_m^{+}, \\ H_1^{+} &\approx W_2^{\pm} \cdots W_m^{\pm} H_m^{+}. \end{aligned} \tag{3}$$

The implicit representations $(H_1^{+}, \ldots, H_{m-1}^{+})$ are also restricted to be nonnegative. Therefore, each layer of this hierarchy of representations also lends itself to be a clustering interpretation. By doing this, the model can find low-dimensional representations of the input data matrix. In [36], the Deep Semi-NMF model is able to outperform the single-layer Semi-NMF in a human face identification task. In [37], Deep NMF is utilized in speech separation, and the experimental results show that Deep NMF outperforms the single-layer NMF in terms of the source-to-distortion ratio (SDR). This research proved that the low-dimensional representations generated by Deep Semi-NMF are better suited for clustering.

2.1.2. Strategy for Pre-classification

Traditional methods can hardly discriminate change and unchanged pixels directly. Therefore, we aim to use a deep learning-based method to improve the performance of pixel classification. The change detection task is treated as an incremental learning problem in this paper. An initial change map is generated through the pre-classification process. Pixels in the input images are classified into three groups: the changed class Ω_c, the unchanged class Ω_u, and the intermediate class Ω_i. Pixels belonging to Ω_c and Ω_u have high probabilities of being changed and unchanged, respectively. These pixels are

the training samples for SVD networks to generate a classifier. By using the classifier, pixels belonging to Ω_i can be further classified into changed and unchanged. Then, the SVD networks classification result and the pre-classification result can be combined to form the final change map. The intermediate Ω_i class can be viewed as the bridge between the pre-classification stage and the SVD networks classification stage.

In order to deal with the speckle noise in both SAR images, the well-known log-ratio operator [1,14,23] is applied to generate the difference image (DI). Let I_D be the DI, and it can be com-puted pixel by pixel from I_1 and I_2 by:

$$I_D = |\log(I_1) - \log(I_2)|. \tag{4}$$

The log-ratio operator is usually expressed in absolute value form. It is worth noting that the absolute value form is empirically verified to be robust to calibration errors. Based on these considerations, we adopt the log-ratio operator in the proposed change detection method.

After obtaining the difference image, the next step is to extract features by using Deep Semi-NMF. Neighborhood patches of the size $h \times h$ pixels around each pixel are extracted and these patches are rearranged as column vectors. Then, the column vectors for all the pixels are combined to form a $h^2 \times MN$ data matrix V. The process of data matrix V generation is illustrated in Figure 2.
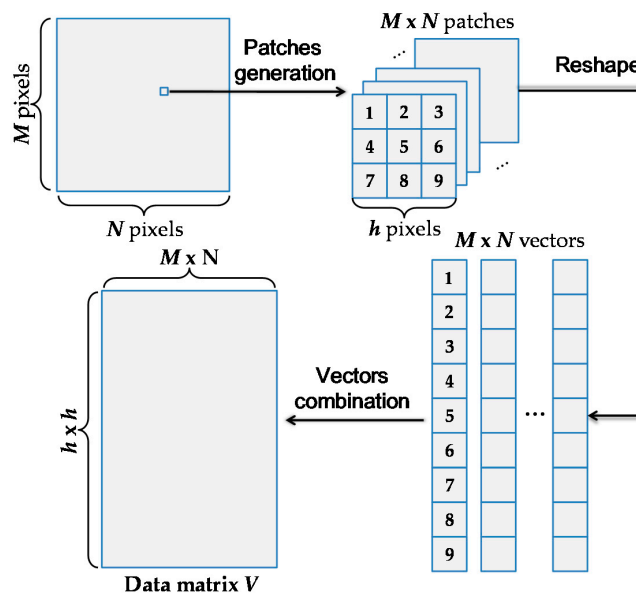

Figure 2. Flow diagram of data matrix V generation.

The factorization algorithm starts from W_0 and H_0, where usually W_0 and H_0 are randomly initialized matrices. Here, to speed up the convergence rate of NMF, Nonnegative Double Singular Value decomposition (NNDSVD) is used. Another important issue that can affect the performance of pre-classification is the structure of Deep Semi-NMF. As empirically verified in [36], the two-layer model is generally sufficient to achieve good performance, and a higher number of layers does not seem to lead to significant improvements. Therefore, we implement Deep Semi-NMF with a first hidden representation H_1 with $\lceil 2h^2/3 \rceil$ features, and a second representation H_2 with $\lceil h^2/2 \rceil$ features. $\lceil \ \rceil$ is the mathematical ceiling operator that maps a real number to the smallest following integer.

H_2 is a matrix with $h^2/2$ rows and MN columns. The matrix denotes the low-dimensional representation of all the pixels in the DI. Then we implement the FCM algorithm on the matrix to partition the pixels in the DI into three groups: the changed class Ω_c, the unchanged class Ω_u, and the intermediate class Ω_i. Pixels belonging to Ω_c have a high probability of being changed, and pixels belonging to Ω_u have a high probability of being unchanged. Therefore, these two kinds of pixels

can be chosen as samples. We use the hierarchical FCM clustering algorithm [38] for classification. We observed that if we directly classify pixels into three classes by FCM, the intermediate class often occupies a large part, and then we can hardly obtain enough representative samples for SVD networks training. Therefore, the FCM algorithm is organized in a cascade way to implement a coarse-to-fine procedure to guarantee efficiency. Finally, we obtain the pre-classification change map with labels $\{\Omega_c, \ \Omega_i, \ \Omega_u\}$. Pixels belonging to Ω_c and Ω_u are selected as training samples.

The number of samples is a critical issue for the classification task. In our implementations, 8% of pixels from Ω_c and Ω_u are randomly selected as training samples. Moreover, we have empirically observed that these training samples are in general sufficient to achieve good performance and that more training samples do not necessarily lead to further improvement. In the next subsection, we will describe how to classify the pixels belonging to Ω_i.

2.2. Classification by Using SVD Networks

In order to accurately identify the changed regions between multi-temporal SAR images, the analysis of the nonlinear relations from both input images is very important. In this paper, SVD networks are utilized as the classifier. The merits of SVD networks lay in the fact that features are not designed by human engineers but are learnt from the image raw data by hierarchical structures. Thus, SVD networks are able to obtain better interpretations of the nonlinear relations from the image raw data.

The structure of SVD networks is shown in Figure 3. In the SVD filter convolutional stage, we use two convolutional layers. In the feature generation and classification stage, hash coding and linear SVM classifier are utilized. In the next subsections, we will give a detailed introduction of the two stages of SVD networks.
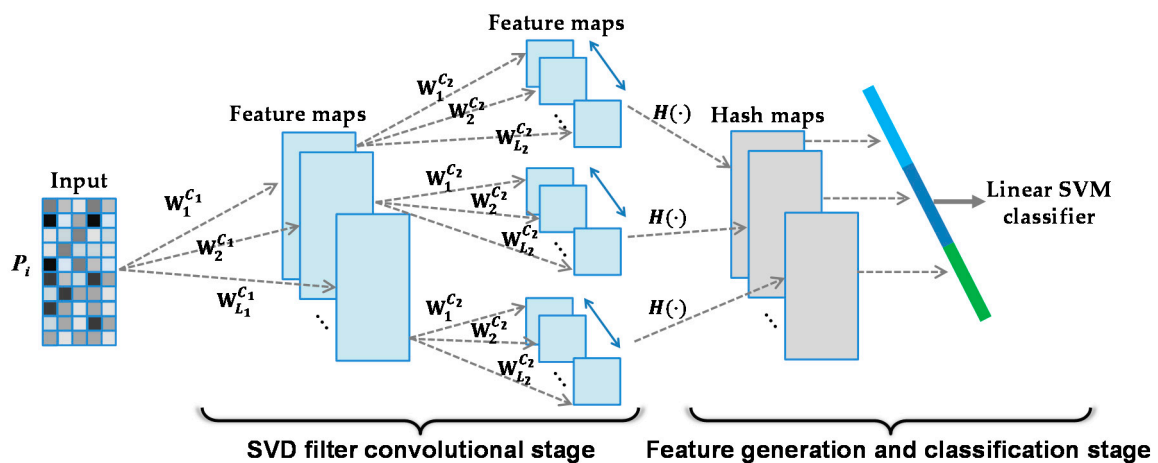

Figure 3. Detailed block diagram of singular value decomposition SVD networks.

2.2.1. Stage 1: SVD Filter Convolutional Stage

In the SVD filter convolutional stage, sample image patches around sample pixels (belonging to Ω_c and Ω_u) are generated first. The sample image patches generation process is shown in Figure 4. These patches contain local change information at the same positions. In image I_1, the sample patch at the central pixel $I_1(m,n)$ is defined as $P_{mn}^{I_1} = \{I_1(\text{row, col}) \big| m - l \leq \text{row} \leq m + l, \ n - l \leq \text{col} \leq n + l\}$, $l = (k-1)/2$. The size of $P_{mn}^{I_1}$ is $k \times k$. At the same time, the corresponding sample patch in image I_2 at the central pixel $I_1(m,n)$ is defined as $P_{mn}^{I_2} = \{I_2(\text{row, col}) \big| m - l \leq \text{row} \leq m + l, \ n - l \leq \text{col} \leq n + l\}$. Both patches are concatenated into a new image patch P_{mn}, and the size of P_{mn} is $2k \times k$. We randomly choose N samples to obtain the sample images P_i, $i = 1, 2, 3, \cdots, N$.
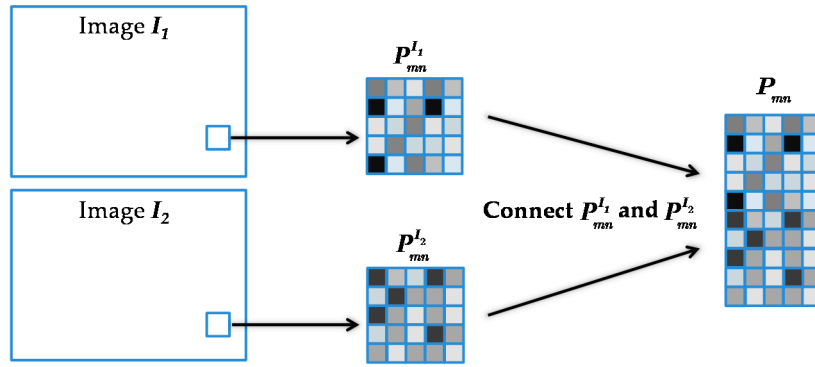
Figure 4. Neighborhood patches generation process.

After sample image patches generation, we obtain N sample images P_i, $i = 1, 2, 3, \cdots, N$. These image patches are fed into two SVD convolutional layers. The filter banks of the first and second convolutional layers are denoted as:

$$
\begin{aligned}
&W_m^{C1} \in \mathbb{R}^{2k \times k}, m = 1, 2, \cdots, L_1, \\
&W_n^{C2} \in \mathbb{R}^{2k \times k}, n = 1, 2, \cdots, L_2,
\end{aligned}
\tag{5}
$$

where L_1 and L_2 represent the number of filters in the first and second convolutional layers, respectively. The mth output map of the first convolutional layer can be denoted as:

$$
\mathcal{F}_{i_m}^1 = P_i \times W_m^{C1}, m = 1, 2, \cdots, L_1, i = 1, 2, \cdots, N
\tag{6}
$$

Then, the output map of the second convolution layer can be represented as:

$$
\mathcal{F}_{i_{mn}}^2 = \mathcal{F}_{i_m}^1 \times W_n^{C2}, m = 1, 2, \cdots, L_1, \ n = 1, 2, \cdots, L_2, i = 1, 2, \cdots, N
\tag{7}
$$

We use L_1 primary filters in the first convolutional layer, and then we obtain L_1 feature maps. In the second convolutional layer, each feature map is an individual input, and the output can be regarded as L_1 groups of features maps. Since we use L_2 primary filters in the second convolutional layer, we obtain $L_1 \times L_2$ feature maps in total. SVD networks are utilized as the filters to obtain the feature maps, and they are capable of exploiting the abstract semantics of the image data. Next, we give a brief review of the SVD algorithm and then introduce how SVD is used in the two convolutional layers.

SVD is a simple yet effective algorithm for extracting the dominant features by projecting the original high dimensional space into low semantic dimensional space. Compared with other feature reduction methods or feature learning methods, such as linear discriminant analysis and principal component analysis, SVD makes use of the relationships between features to establish underlying semantic means. An enriched feature space with a small number of features is established to represent the original data. Therefore, SVD can not only reduce the dimensionality, but also improve the feature classification performance. Deep learning methods may perform poorly when the number of training samples is relatively small. However, it is nearly impossible for the task of SAR image change detection to obtain tens of millions of training samples. We select SVD as the convolutional filter because it is theoretically sound, robust, and structurally compact. It is empirically verified that it performs better than principal component analysis and linear discriminant analysis.

As mentioned above, in the process of sample image patches generation, we obtain N sample images P_i, $i = 1, 2, 3, \cdots, N$. In the first convolutional layer, the pixels of each sample image are reshaped into a vector $p_i^{C1} \in \mathbb{R}^{2k^2 \times 1}$, and all the vectors are combined into a matrix

$P_{C1} = [p_1^{C1}, \ p_2^{C1}, \ \cdots, \ p_N^{C1}] \in \mathbb{R}^{2k^2 \times N}$. Then, the SVD of the data matrix P_{C1} is a factorization as follows:

$$P_{C1} = U_{C1} \sum\nolimits_{C1} V_{C1}^T \tag{8}$$

where $\sum_{C1}$ is a rectangular diagonal matrix with nonnegative real numbers on its diagonal. The diagonal entries of $\sum_{C1}$ are known as the singular values of P_{C1}. $U_{C1} \in \mathbb{R}^{2k^2 \times 2k^2}$ and $V_{C1} \in \mathbb{R}^{N \times N}$ are two orthogonal matrices. The columns of U_{C1} are called the left-singular vectors of P_{C1}, and the columns of V_{C1} are called the right-singular vectors of P_{C1}. In this paper, the left-singular vectors of U_{C1} with the largest L_1 singular values are selected as the primary filter banks of the $C1$ layer.

The filter banks W_i^{C1} can be obtained by reforming $\hat{u}_i^{C1}$ back into the 2-D filters.

In the $C2$ layer, the input is $N \times L_1$ feature maps. The feature maps are reshaped into a vector p_i^{C2}, $i = 1, 2, 3, \cdots, N \times L_1$. All vectors are combined into a data matrix $P_{C2} = [p_1^{C2}, \ p_2^{C2}, \ \cdots, \ p_{NL_1}^{C2}] \in \mathbb{R}^{2k^2 \times NL_1}$. Therefore, the data matrix P_{C2} is factorized as follows:

$$P_{C2} = U_{C2} \sum\nolimits_{C2} V_{C2}^T \tag{9}$$

where $\sum_{C2}$ is a rectangular diagonal matrix containing singular values of P_{C2}. U_{C2} is an orthogonal matrix containing left-singular vectors of P_{C2}. V_{C2} is an orthogonal matrix containing right-singular vectors of P_{C2}. Similar to the first convolutional layer, the left-singular vectors of U_{C2} with the largest L_2 singular values are selected as the primary filter banks of the $C2$ layer. The filter banks W_i^{C2} are obtained by reforming $\hat{u}_i^{C2}$ back into the 2-D filters.

2.2.2. Stage 2: Feature Generation and Classification Stage

Through two convolutional layers, we obtain $N \times L_1$ group outputs, and each group contains L_2 feature maps. Then, each feature map is binarized using a Heaviside step function whose value is one for positive input and zero otherwise. Then, in each group of feature maps, around the same position we have L_2 binary bits. For the mth group of the L_2 binary bits, they can be encoded into a decimal number as follows:

$$D_m = \sum\nolimits_{n=1}^{L_2} 2^{n-1} H\left(\mathcal{F}_{i_{mn}}^2\right), \ \ m = 1, \ 2, \cdots, L_1, i = 1, \ 2, \cdots, N \tag{10}$$

Then, the output feature maps $\mathcal{F}_{i_{mn}}^2$ are converted into L_1 groups of integer-valued "images" D_m, where the value of each pixel is in the range $\left[0, \ 2^{L_2} - 1\right]$. Then, the histogram of D_m are calculated, and form a feature vector $\text{Hist}(D_m)$. Finally, all the feature vectors of the same group are further concatenated together to form the final change map to form the final feature descriptor of the input image P_i, i.e.,

$$\text{FEAT}(P_i) = [\text{Hist}(D_1); \ \text{Hist}(D_2); \ \cdots; \ \text{Hist}(D_{L_1})]. \tag{11}$$

Then, the feature descriptors of all the sample images are fed into the linear SVM to train a model. By using the model, pixels belonging to Ω_i are further separated into changed and unchanged classes. Finally, we combine the SVD networks classification result and the pre-classification result together to form the final change map. We have tried different numbers of layers in the SVD networks. From the experimental results, we have found that two layers for feature extraction is sufficient to achieve good performance. Therefore, in our implementations, we set the number of layers for feature extraction to two. Moreover, the SVD filter number L_1 and L_2 also affects the classification performance slightly when L_1 and L_2 are set larger than six. Inspired by Gabor filters and histogram of oriented gradients (HOG), the common settings of filters often have eight orientations, therefore, L_1 and L_2 are set as eight in our implementations.

3. Experimental Results and Analysis

In this part, Section 3.1 briefly introduces the SAR datasets used in our experiments, and then describes the criterions that should be considered in performance assessment. Finally, the proposed method is compared with closely related methods on three SAR datasets. The methods used for comparison purpose are principal component analysis and k-means clustering (PCAKM) [18], improved FCM algorithm based on Markov random field (MRFFCM) [39], Gabor feature with two-level clustering (GaborTLC) [19], and deep neural networks with MRFFCM preclassification (D_MRFFCM) [22]. The results of PCAKM, MRFFCM, GaborTLC are implemented by using the authors' publicly available code.

3.1. Dataset Description and Experimental Settings

In order to evaluate the effectiveness of the proposed method, we apply the proposed method to three real multi-temporal SAR datasets acquired by different sensors. Co-registration and geometric corrections have been done on these datasets before applying the proposed method. As mentioned in [1], the ground truth change map is very important for accuracy assessment of the change detection performance. An inaccurate ground truth change map will lead to improper assessments. Therefore, in this paper, the ground truth images were created by manual annotation, which combines on-the-spot investigation and expert knowledge.

The first dataset is the Yellow River dataset. It presents a section of SAR images acquired by Radarsat-2 at the region of the Yellow River Estuary in China. The original SAR image is shown in Figure 5. We select one representative area of size 257×289 for change detection. The image acquired in 2008 is shown in Figure 6a, while the image acquired in 2009 is shown in Figure 6b. The ground truth change map is shown in Figure 6c, and it was generated by on-the-spot investigation and expert knowledge. It should be noted that the two images are a single-look image and a four-look image. Therefore, the influence of speckle noise in the dataset is much greater than the other datasets.
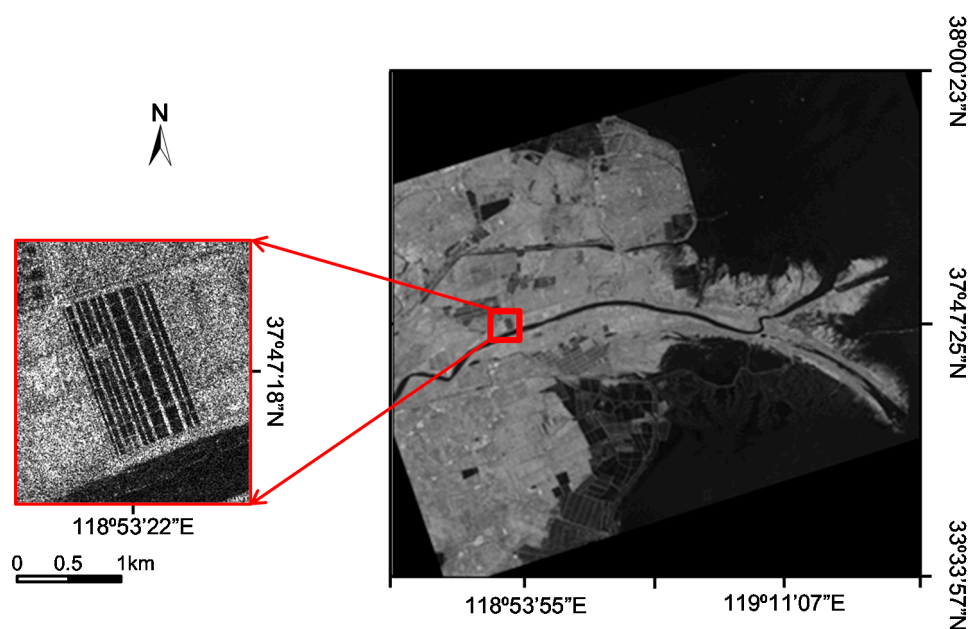

Figure 5. SAR images acquired by Radarsat-2 over the Yellow River Estuary in China.
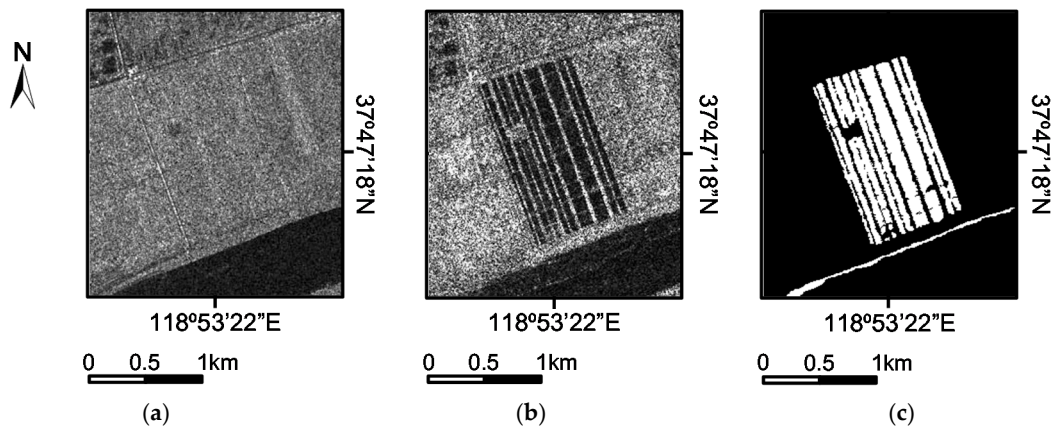
Figure 6. Yellow River dataset. (**a**) Image acquired in 2008. (**b**) Image acquired in 2009. (**c**) Ground truth change map created by on-the-spot investigation and expert knowledge.

The second dataset is the San Francisco dataset. It presents a section (256×256 pixels) of two SAR images acquired by the ERS-2 SAR sensor over the city of San Francisco. The original images are 7749×7713 pixels, as shown in Figure 7. The images are provided by the European Space Agency. The image captured in August 2003 is shown in Figure 8a, and the image captured in May 2004 is shown in Figure 8b. The ground truth change map is shown in Figure 8c, and it was generated by integrating prior information with photo interpretation.
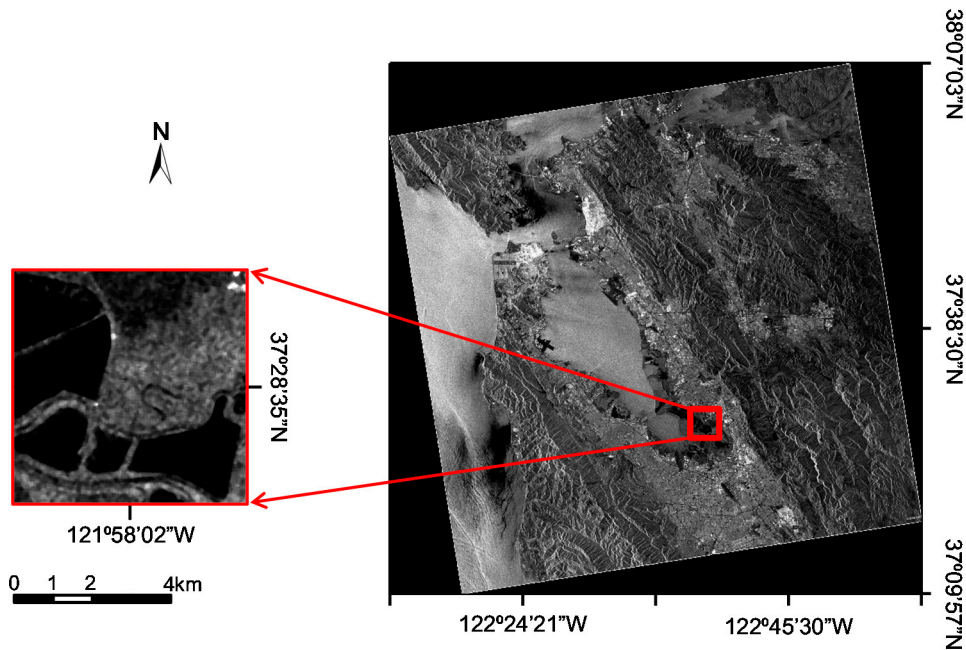

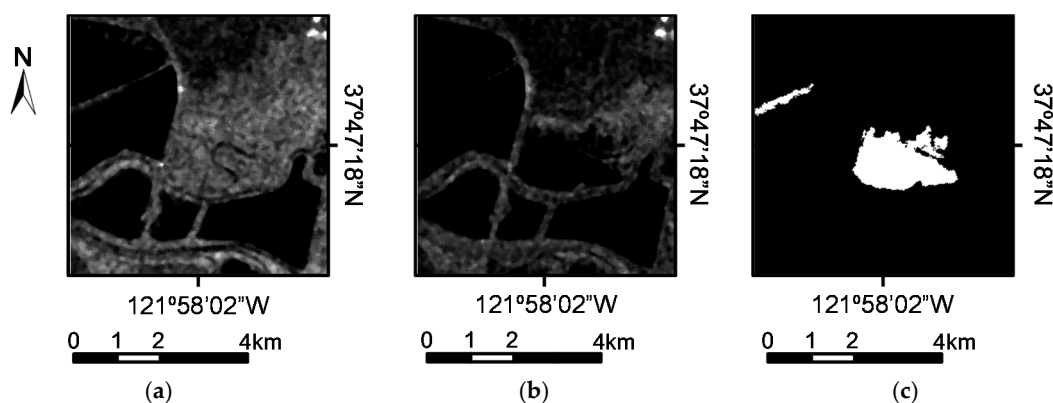**Figure 7.** SAR images acquired by ERS-2 over the city of San Francisco.

Figure 8. San Francisco dataset. (**a**) Image acquired in August 2003. (**b**) Image acquired in May 2004. (**c**) Ground truth change map created by integrating prior information with photo interpretation.

The third dataset, as shown in Figure 9, is the Ottawa dataset. It represents a section (290 × 350 pixels) of two SAR images over the city of Ottawa. The images are captured in May 1997 and August 1997, respectively, by the RADARSAT SAR sensor. The dataset was provided by Defense Research and Development Canada, Ottawa. The images present changed areas that were once afflicted by floods. The ground truth image, shown in Figure 9c, was created by on-the-spot investigation and expert knowledge. It is worth noting that the Yellow River dataset and the San Francisco dataset represent changed areas generated by newly irrigated farmlands, while the Ottawa dataset represents changed areas that were once afflicted by floods.
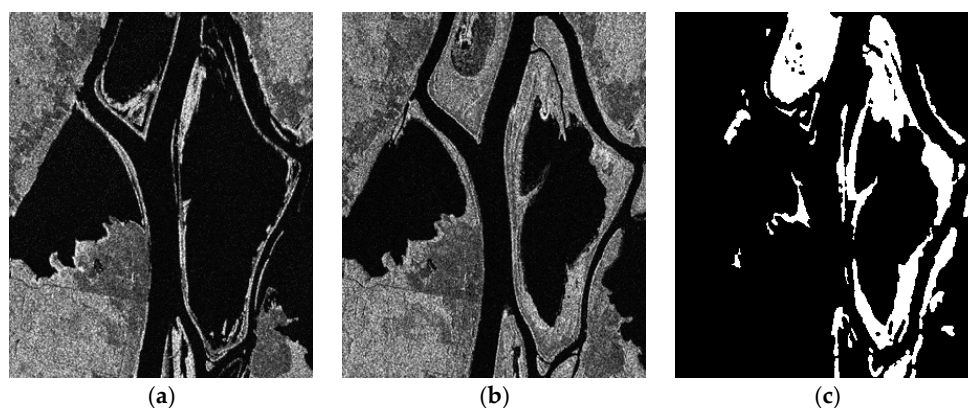

Figure 9. Ottawa dataset. (**a**) Image acquired in May 1997. (**b**) Image acquired in August 1997. (**c**) Ground truth change map created by on-the-spot investigation and expert knowledge.

The performance evaluation of SAR image change detection is a critical issue. Both visual and quantitative analyses are made in our experiments. In the visual analysis, we compare the binary change map generated by each method with the ground truth change map. For quantitative analysis, we compute five criteria for each change map: false positives (FP), false negatives (FN), overall errors (OE), percentage correct classification (PCC), and Kappa coefficient (KC). FP denotes the number of pixels belonging to the unchanged class that are wrongly classified as part of the changed class, whereas FN denotes the number of pixels belonging to the changed class that are wrongly classified into the unchanged class. OE can be obtained by using $OE = FP + FN$. In the binary ground truth change map, we count the actual number of pixels belonging to the changed class and the unchanged class. The number of pixels belonging to the changed class is denoted by Nc, while the number of pixels belonging to the unchanged class is denoted by Nu. Next, PCC is computed by

$\text{PCC} = (Nu + Nc - \text{FP} - \text{FN})/(Nu + Nc) \times 100\%$. KC gives the percentage of agreement (correct classified pixels) corrected by the number of agreements that would be expected purely by chance. To be specific, KC is defined as:

$$\text{KC} = (\text{PCC} - \text{PRE})/(1 - \text{PRE}), \tag{12}$$

where

$$\text{PRE} = \frac{(Nc + \text{FP} - \text{FN}) \times Nc + (Nu + \text{FN} - \text{FP}) \times Nu}{(Nc + Nu) \times (Nc + Nu)}. \tag{13}$$

It should be noted that PCC relies only on the sum values of FP and FN, whereas KC relies on the dependent values of FP and FN. As mentioned in [39], more detailed information is involved in KC, and thus KC is a more persuasive coefficient than PCC. It is well worth noting that the receiver operating characteristic (ROC) evaluation is usually a comprehensive metric in change detection [23]. It can evaluate the intrinsic quality of change detection independent of the threshold choice. However, the proposed method is a classification-based method. Therefore, there is no threshold to be tuned when generating the change detection map. It is hard to perform the ROC evaluation against the comparison methods. The ROC evaluation is not provided in our experiments.

The proposed method is compared with closely related methods on three SAR datasets. The methods used for comparison purpose are PCAKM, MRFFCM, and GaborTLC. The results of PCAKM, MRFFCM and GaborTLC are implemented by using the authors' publicly available code. Then, these methods are implemented using the default parameters provided in the source codes. In PCAKM, the block size is set to 5. In MRFFCM, the number of subintervals is set to 30, as mentioned in [39]. In GaborTLC, $U = 8$, $f = \sqrt{2}$, and $V = 5$ are used. It should be noted that since we could not find the author's source code of D_MRFFCM, we implement D_MRFFCM by ourselves in MATLAB.

3.2. Experiemental Results on the Yellow River Dataset

As aforementioned, both visual and quantitative analyses are made in our experiments. With respect to the visual analysis, the final change maps on the three datasets are exhibited in figure form. For quantitative analysis, the final change maps are exhibited in tabular form.

Figure 10 presents the change maps generated by different methods on the Yellow River dataset. The corresponding quantitative metrics on the change maps generated by different methods are shown in Table 1. As shown in Figure 10a, PCAKM wrongly classifies many unchanged pixels into the changed class, which results in a noisy change map. Therefore, the FP value of PCAKM is listed as the maximum value in Table 1. The MRFFCM and GaborTLC methods work well in suppressing the unchanged regions, but many changed regions are wrongly detected as unchanged ones. Hence, the FN value of MRFFCM and GablorTLC are listed as high values in Table 1. By contrast, the proposed method achieves the maximum KC value. It should be noted that the PCC value obtained by D_MRFFCM is slightly higher than the proposed method. However, the proposed method can draw a balance between FP and FN, and therefore the KC value of the proposed method is better than D_MRFFCM. As mentioned above, KC is a more persuasive coefficient than PCC. Thus we can draw the conclusion that the proposed method outperforms the other methods and indeed has the ability to improve the change detection accuracy.
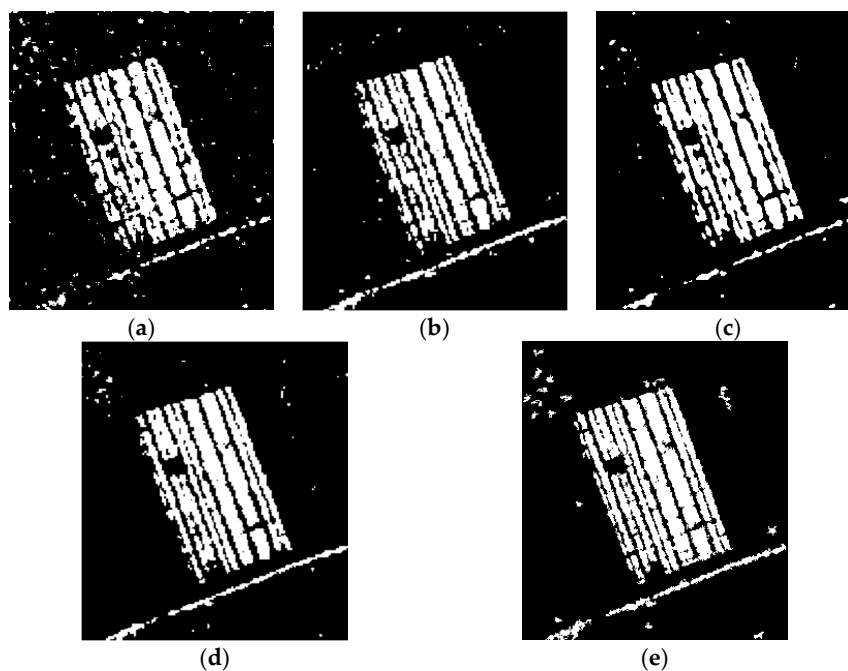
Figure 10. Change detection results generated by different methods on the Yellow River dataset.
(**a**) Result by PCAKM. (**b**) Result by MRFFCM. (**c**) Result by GaborTLC. (**d**) Result by D_MRFFCM.
(**e**) Result by the proposed method.

Table 1. Change detection results of different methods on the Yellow River dataset.

Methods	False Positives (FP)	False Negatives (FN)	Overall Errors (OE)	Percentage Correct Classification (PCC)	Kappa Coefficient (KC)
PCAKM	2137	2663	4800	93.54	77.85
MRFFCM	640	2974	3614	95.13	82.38
GaborTLC	1159	2312	3471	95.33	83.68
D_MRFFCM	656	2676	3332	95.51	83.92
Proposed method	1748	1647	3395	95.43	84.62

3.3. Experimental Results on the San Francisco Dataset

Figure 11 shows the change maps generated by different methods on the San Francisco dataset. The corresponding quantitative metrics on the change maps generated by different methods are shown in Table 2. From the visual comparison among the change maps, we find that PCAKM, MRFFCM, GaborTLC and D_MRFFCM generate many noise regions, and in these regions many unchanged pixels are falsely classified into the changed class. Therefore, the FP values of these methods are relatively high. Compared with other methods, the proposed method achieves much better change maps, and it performs well at suppressing noisy unchanged pixels. The comparison shows that employing SVD networks for feature representation is beneficial to suppress noisy unchanged pixels while amplifying the key changed regions.
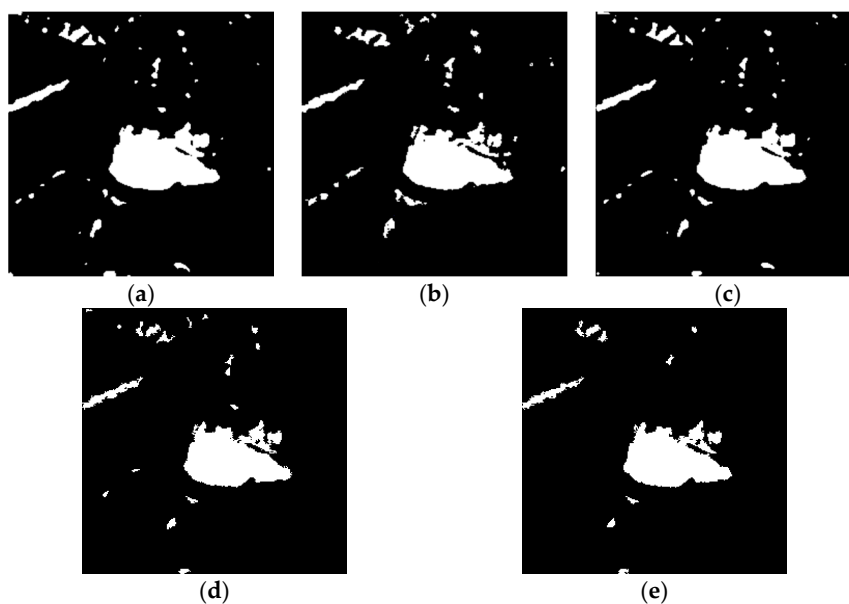
Figure 11. Change detection results generated by different methods on the San Francisco dataset. (**a**) Result by PCAKM. (**b**) Result by MRFFCM. (**c**) Result by GaborTLC. (**d**) Result by D_MRFFCM. (**e**) Result by the proposed method.

Table 2. Change detection results of different methods on the San Francisco dataset.

Methods	FP	FN	OE	PCC (%)	KC (%)
PCAKM	1618	25	1643	97.49	83.68
MRFFCM	1511	191	1702	97.40	82.69
GaborTLC	1376	60	1436	97.81	85.39
D_MRFFCM	676	192	868	98.68	90.48
Proposed method	157	573	730	98.89	91.25

3.4. Experimental Results on the Ottawa Dataset

Figure 12 shows the final change maps of different methods on the Ottawa dataset, while Table 3 lists the values for quantitative analysis. Table 3 shows that for MRFFCM and D_MRFFCM, some unchanged pixels are falsely classified into the changed class, and thus MRFFCM and D_MRFFCM suffer from high FP values. In Figure 12a,c, we can observe that some changed pixels are missed in the change maps generated by PCAKM and GaborTLC. Therefore, the FN values of PCAKM and GaborTLC are relatively high. The proposed method achieves the best PCC and KC values, which demonstrates that the SVD networks effectively exploit the nonlinear relations from the original data. Both visual and quantitative comparisons demonstrate the effectiveness of the proposed method for change detection on the dataset.
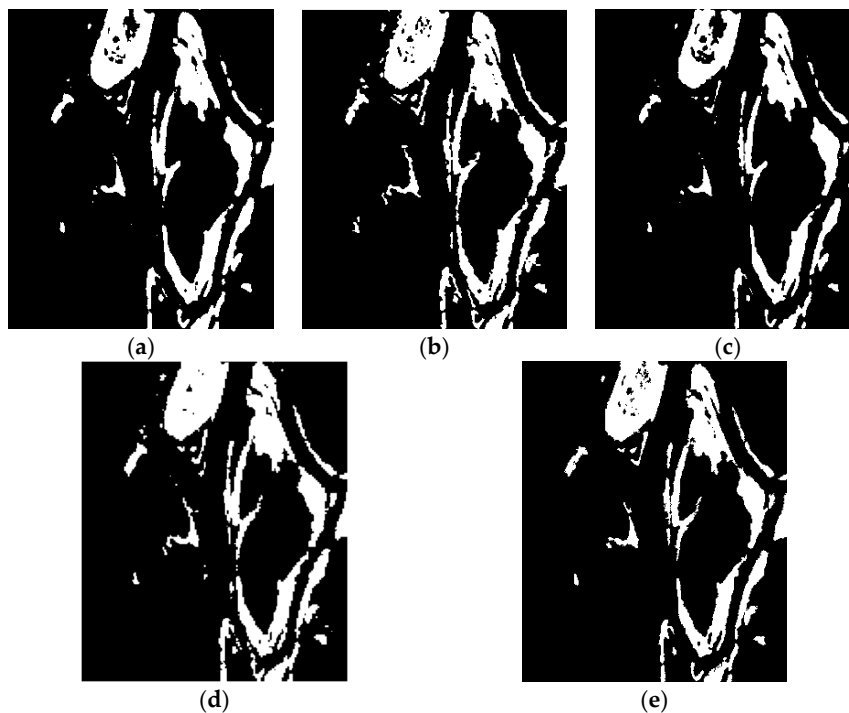
Figure 12. Change detection results generated by different methods on the Ottawa dataset. (**a**) Result by PCAKM. (**b**) Result by MRFFCM. (**c**) Result by GaborTLC. (**d**) Result by D_MRFFCM. (**e**) Result by the proposed method.

Table 3. Change detection results of different methods on the Ottawa dataset.

Methods	FP	FN	OE	PCC (%)	KC (%)
PCAKM	960	1515	2475	97.56	90.43
MRFFCM	1636	712	2348	97.69	91.27
GaborTLC	253	2531	2784	97.26	88.71
D_MRFFCM	994	704	1699	98.33	93.58
Proposed method	550	1074	1624	98.40	93.73

4. Discussion

4.1. Parameter Selection and Sensitivity Analysis

The ideal parameter for change detection should be selected before verifying the effectiveness of the proposed method. In SVD networks, the size of the sample image patch is an important parameter, since the local information is sensitive to neighborhood noise. Therefore, the first experiment is a test of parameter k, which denotes the size of the sample image patch from each input SAR image. We evaluate the performance of change detection by taking $k = 3, 5, 7, 9, 11$, and 13, respectively. The PCC value is exploited as the validation criterion on different datasets. Figure 13 shows the sensitivity analysis results of the sample image patch size k. The curves in different colors denote the results on different datasets.
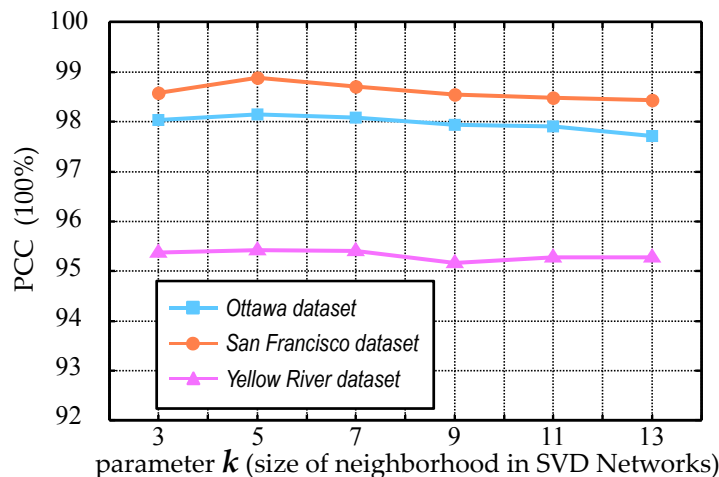
Figure 13. Relationship between PCC and the parameter *k* on three SAR datasets.

The PCC values of the proposed method on the three datasets begin to decrease when $k \geq 7$, and this denotes that the sample image patches are not representative of the specified position. When $k = 5$, the proposed method achieves the best performance on three datasets. Therefore, in our implementations, *k* is set to 5 for the sample image patches in the SVD networks.

Solving the high dimensional feature classification problem is crucial in this paper. We have two choices: LIBLINEAR [40] and LIBSVM [41]. Both software packages are designed for the efficient classification of large-scale data. We have conducted several experiments on LIBLINEAR and LIBSVM, and we found that LIBLINEAR is about 20% faster than LIBSVM. Thus, we use LIBLINEAR in the proposed method as classifier.

4.2. Comparison

The main objective of the proposed method is to detect change between multi-temporal SAR images. As shown in Tables 1–3, the proposed method is compared with closely related methods on three SAR datasets. The methods used for the purpose of comparison are PCAKM, MRFFCM, GaborTLC and D_MRFFCM.

From the experimental results on the three datasets, the proposed method obtains the maximum KC values and the smallest OE values. It is evident that the proposed method is more robust to the speckle noise by extracting representative features for each pixel by using SVD networks. Therefore, the OE yielded by the proposed method is much lower. In addition, it should be noted that the value of KC is the most cogent and discriminative criterion for change detection. The KC value of the proposed method is the best on all these three datasets. Thus, the proposed method outperforms all the other methods, and efficiently improves the change detection performance. Moreover, from Tables 1–3, we can observe that the proposed method is able to find a balance between FP and FN. It demonstrates that the SVD networks can effectively exploit the nonlinear relations from the original data, and therefore can suppress the noisy unchanged regions while preserving details.

PCAKM and MRFFCM utilize single K-means and FCM clustering for change detection, respectively. It is hardly enough for both methods to generate satisfying results, since a cascade scheme is necessary for a change detection model with high classification power. GaborTLC obtains good performance by using a two-layer classification model. Nevertheless, it is of less discrimination power compared with D_MRFFCM and the proposed method. This is owing to the reason that D_MRFFCM and the proposed methods use deep learning-based models. Therefore, both methods can automatically obtain more representative semantic features in a hierarchical manner. The proposed method performs better D_MRFFCM. This is because D_MRFFCM requires tens of millions of training

samples for training, which is nearly impossible to obtain for the task of SAR image change detection. The proposed method is a lightweight model and performs well with relatively fewer samples.

5. Conclusions

In this paper, we proposed a novel SAR image change detection method based on Deep Semi-NMF and SVD Networks. In the proposed method, Deep Semi-NMF is used for pre-classification, and reliable samples of high accuracy can be obtained. In addition, nonlinear relations of multi-temporal SAR images can be exploited by SVD networks. We use two SVD convolutional layers to obtain reliable features, which effectively improve the classification performance. The proposed method makes no rigorous assumption and is unsupervised. Therefore, it can be easily adapted for data across different SAR sensors. The experimental results have demonstrated the effectiveness of the proposed method on three SAR image datasets.

The proposed method is a promising tool to detect changed regions for multi-temporal SAR images. However, it is still challenging to change point targets, such as aircrafts at an airport and cars in a parking lot. Therefore, in the future, we will conduct research on detecting change point targets. In addition, as more and more multisource remote sensing data covering the same area are available, it is demanding to develop change detection techniques for multisource data. Therefore, we will continue to investigate the proposed method to detect changes from multisource data. Moreover, if a series of multi-temporal SAR images are used for change detection, the spatial and temporal dynamics of a specified region can be obtained. The spatial and temporal dynamics can provide predictions of likely changes in the future. They can also provide intricate information for effective planning and management activities. In the future, we will continue our work on investigating change detection by using a series of multi-temporal SAR images.

Author Contributions: Feng Gao and Xiaopeng Liu proposed the original idea and designed the study. Junyu Dong, Guoqiang Zhong, and Muwei Jian contributed to the discussion of the results. Feng Gao wrote the manuscript which was revised by all authors.

Conflicts of Interest: The authors declare no conflict of interest.

References

1. Shao, P.; Shi, W.; He, P.; Hao, M.; Zhang, X. Novel approach to unsupervised change detection based on a robust semi-supervised FCM. *Remote Sens.* **2016**, *8*, 264. [CrossRef]
2. Navarro, A.; Rolim, J.; Miguel, I.; Catalão, J.; Silva, J.; Painho, M.; Vekerdy, Z. Crop monitoring based on SPOT-5 take-5 and Sentinel-1A data for the estimation of crop water requirements. *Remote Sens.* **2016**, *8*, 525. [CrossRef]
3. Tewolde, M.G.; Cabral, P. Urban sprawl analysis and modeling in Asmara, Eritrea. *Remote Sens.* **2011**, *3*, 2148–2165. [CrossRef]
4. Yang, Y.; Wong, L.; Chen, C.; Chen, T. Using multi-temporal Landsat imagery to monitor and model the influence of landscape pattern on urban expansion in a metropolitan region. *J. Appl. Remote Sens.* **2014**, *8*, 083639. [CrossRef]
5. Othman, A.A.; Gloaguen, R. River Courses Affected by landslides and implications for hazard assessment: A high resolution remote sensing case study in NE Iraq–W Iran. *Remote Sens.* **2013**, *5*, 1024–1044. [CrossRef]
6. Pettinato, S.; Santi, E.; Paloscia, S.; Aiazzi, B. Snow cover area identification by using a change detection method applied to COSMO-SkyMed images. *J. Appl. Remote Sens.* **2014**, *8*, 084684. [CrossRef]
7. Hussain, M.; Chen, D.; Cheng, A.; Wei, H.; Stanley, D. Change detection from remotely sensed images: From pixel-based to object-based approaches. *ISPRS J. Photogramm. Remote Sens.* **2013**, *80*, 91–106. [CrossRef]

8. Hou, B.; Wei, Q.; Zheng, Y.; Wang, S. Unsupervised change detection in SAR image based on Gauss-log ratio image fusion and compressed projection. *IEEE J. Sel. Top. Appl. Earth Obs. Remote Sens.* **2014**, *7*, 3297–3317. [CrossRef]

9. Hu, H.; Ban, Y. Unsupervised change detection in multi-temporal SAR images over large urban areas. *IEEE J. Sel. Topics Appl. Earth Obs. Remote Sens.* **2014**, *7*, 3248–3261. [CrossRef]

10. Wang, Y.; Du, L.; Dai, H. Unsupervised SAR image change detection based on SIFT keypoints and region information. *IEEE Geosci. Remote Sens. Lett.* **2016**, *13*, 931–935. [CrossRef]

11. Bujor, F.; Trouve, E.; Valet, L.; Nicolas, J.-M.; Rudant, J.-P. Application of log-cumulants to the detection of spatiotemporal discontinuities in multi-temporal SAR images. *IEEE Trans. Geosci. Remote Sens.* **2004**, *42*, 2073–2084. [CrossRef]

12. Inglada, J.; Mercier, G. A new statistical similarity measure for change detection in multi-temporal SAR images and its extension to multiscale change analysis. *IEEE Trans. Geosci. Remote Sens.* **2007**, *45*, 1432–1445. [CrossRef]

13. Bruzzone, L.; Prieto, D.F. Automatic analysis of the difference image for unsupervised change detection. *IEEE Trans. Geosci. Remote Sens.* **2000**, *38*, 1171–1182. [CrossRef]

14. Bazi, Y.; Bruzzone, L.; Melgani, F. An unsupervised approach based on the generalized Gaussian model to automatic change detection in multi-temporal SAR images. *IEEE Trans. Geosci. Remote Sens.* **2005**, *43*, 874–887. [CrossRef]

15. Celik, T. A Bayesian approach to unsupervised multiscale change detection in synthetic aperture radar images. *Signal Process.* **2010**, *90*, 1471–1485. [CrossRef]

16. Gong, M.; Li, Y.; Jian, L.; Jia, M.; Su, L. SAR change detection based on intensity and texture changes. *ISPRS J. Photogramm. Remote Sens.* **2014**, *93*, 123–135. [CrossRef]

17. Gong, M.; Zhou, Z.; Ma, J. Change detection in synthetic aperture radar images based on image fusion and fuzzy clustering. *IEEE Trans. Image Process.* **2012**, *21*, 2141–2151. [CrossRef] [PubMed]

18. Celik, T. Unsupervised change detection in satellite images using principal component analysis and-means clustering. *IEEE Geosci. Remote Sens. Lett.* **2009**, *6*, 772–776. [CrossRef]

19. Li, H.C.; Celik, T.; Longbotham, N.; Emery, W.J. Gabor feature based unsupervised change detection of multi-temporal SAR images based on two-level clustering. *IEEE Geosci. Remote Sens. Lett.* **2015**, *12*, 2458–2462.

20. Lv, P.; Zhong, Y.; Zhao, J.; Jiao, H.; Zhang, L. Change detection based on multifeature probabilistic ensemble conditional random field model for high spatial resolution remote sensing imagery. *IEEE Geosci. Remote Sens. Lett.* **2016**, *13*, 1965–1969. [CrossRef]

21. Liu, J.; Gong, M.; Zhao, J.; Li, H.; Jiao, L. Difference representation learning using stacked restricted Boltzmann machines for change detection in SAR images. *Soft Comput.* **2014**, *20*, 4645–4657. [CrossRef]

22. Gong, M.; Zhao, J.; Liu, J.; Miao, Q.; Jiao, L. Change detection in synthetic aperture radar images based on deep neural networks. *IEEE Trans. Neural Netw.* **2016**, *27*, 125–138. [CrossRef] [PubMed]

23. Liu, J.; Gong, M.; Qin, K.; Zhang, P. A deep convolutional coupling network for change detection based on heterogeneous optical and radar images. *IEEE Trans. Neural Netw.* **2017**, *28*, 1–15. [CrossRef] [PubMed]

24. Zhang, P.; Gong, M.; Su, L.; Liu, J.; Li, Z. Change detection based on deep feature representation and mapping transformation for multi-spatial-resolution remote sensing images. *ISPRS J. Photogramm. Remote Sens.* **2016**, *116*, 24–41. [CrossRef]

25. Zhong, Y.; Liu, W.; Zhao, J.; Zhang, L. Change detection based on pulse-coupled neural networks and the NMF feature for high spatial resolution remote sensing imagery. *IEEE Geosci. Remote Sens. Lett.* **2015**, *12*, 537–541. [CrossRef]

26. Zhang, L.; Zhang, L.; Du, B. Deep learning for remote sensing data: A technical tutorial on the state of the art. *IEEE Geosci. Remote Sens. Mag.* **2016**, *4*, 22–40. [CrossRef]

27. Zhang, L.; Zhang, Q.; Zhang, L.; Tao, D.; Huang, X.; Du, B. Ensemble manifold regularized sparse low-rank approximation for multiview feature embedding. *Pattern Recognit.* **2015**, *48*, 3102–3112. [CrossRef]

28. Pan, B.; Shi, Z.; Xu, X. R-VCANet: A new deep learning-based hyperspectral image classification method. *IEEE J. Sel. Top. Appl. Earth Obs. Remote Sens.* **2017**, *5*, 1975–1986. [CrossRef]

29. Zou, Z.; Shi, Z. Ship detection in spaceborne optical image with SVD networks. *IEEE Trans. Geosci. Remote Sens.* **2016**, *54*, 5832–5845. [CrossRef]

30. Lee, D.D.; Seung, H.S. Learning the parts of objects by non-negative matrix factorization. *Nature* **1999**, *401*, 788–791. [PubMed]

31. Liu, R.; Du, B.; Zhang, L. Hyperspectral unmixing via double abundance characteristics constraints based NMF. *Remote Sens.* **2016**, *8*, 464. [CrossRef]

32. Meganem, I.; Deville, Y.; Hosseini, S.; Deliot, P.; Briottet, X. Linear-quadratic blind source separation using NMF to unmix urban hyperspectral images. *IEEE Trans. Signal Process.* **2014**, *7*, 1822–1833. [CrossRef]

33. Huang, S.; Elhoseiny, M.; Elgammal, A.; Yang, D. Improving non-negative matrix factorization via ranking its bases. In Proceedings of the 2014 IEEE International Conference on Image Processing, Paris, France, 27–30 October 2014; pp. 5951–5955.

34. Guillanmet, D.; Vitria, J.; schiele, B. Introducing a weighted non-negative matrix factorization for image classification. *Pattern Recognit. Lett.* **2003**, *14*, 2447–2454. [CrossRef]

35. Ding, C.H.; Li, T.; Jordan, M.I. Convex and semi-nonnegative matrix factorization. *IEEE Trans. Pattern Anal. Mach. Intell.* **2010**, *32*, 45–55. [CrossRef] [PubMed]

36. Trigeorgis, G.; Bousamlis, K.; Zafeiriou, S.; Schuller, B. A deep Semi-NMF model for learning hidden representations. In Proceedings of the 31st International Conference on Machine Learning, Beijing, China, 21–26 June 2014; pp. 1692–1700.

37. Hsu, C.-C.; Chien, J.-T.; Chi, T.-S. Layered nonnegative matrix factorization for speech separation. In Proceedings of the Interspeech 2015, Dresden, Germany, 6–10 September 2015; pp. 628–632.

38. Gao, F.; Dong, J.; Li, B.; Xu, Q.; Xie, C. Change detection from synthetic aperture radar images based on neighborhood-based ratio and extreme learning machine. *J. Appl. Remote Sens.* **2016**, *10*, 046019. [CrossRef]

39. Gong, M.; Su, L.; Jia, M.; Chen, W. Fuzzy clustering with a modified MRF energy function for change detection in synthetic aperture radar images. *IEEE Trans. Fuzzy Syst.* **2014**, *22*, 98–109. [CrossRef]

40. Fan, R.-E.; Chang, K.-W.; Hsieh, C.-J.; Wang, X.-R.; Lin, C.-J. LIBLINEAR: A library for large linear classification. *J. Mach. Learn. Res.* **2008**, *9*, 1871–1874.

41. Chang, C.-C.; Lin, C.-J. LIBSVM: A library for support vector machines. *ACM Trans. Intell. Syst. Technol.* **2011**, *2*, 1–27. [CrossRef]